

Calibration and Characterization of Hyperspectral Imaging Systems Used for Natural Scene Imagery

Nsikak E. Ekpenyong

Department of Physics, Akwa Ibom State University, Uyo, Nigeria
Email: nsikakekpenyong@yahoo.com

How to cite this paper: Ekpenyong, N.E. (2019) Calibration and Characterization of Hyperspectral Imaging Systems Used for Natural Scene Imagery. *Optics and Photonics Journal*, 9, 81-98.

<https://doi.org/10.4236/opj.2019.97009>

Received: May 26, 2019

Accepted: July 19, 2019

Published: July 22, 2019

Copyright © 2019 by author(s) and Scientific Research Publishing Inc.
This work is licensed under the Creative Commons Attribution International License (CC BY 4.0).

<http://creativecommons.org/licenses/by/4.0/>



Open Access

Abstract

Calibration and characterization of focal plane hyperspectral imaging systems play an important role in natural scene imagery. Illumination plays a major role during imaging, as both the camera and electronically tunable filter may suffer low transmission at the ends of the visible spectrum, resulting in a low signal to noise ratio. It is important that the spectral characteristics of the imaging system as well as its geometric properties be well characterized and its radiometric performance known. The aim of this article is to identify the main sources of errors in a common design of focal-plane hyperspectral imaging system and devise ways of compensating for these errors. Calibration and characterization of a focal-plane hyperspectral imaging system include nominal wavelength accuracy analysis. This was carried out by capturing images of a mercury vapour lamp to study principal emission lines in the visible spectrum. The linearity of the hyperspectral imaging system was investigated by recording an input-output function. This was accomplished by comparing signals captured by the hyperspectral imaging system and luminance data recorded using a luminance meter. System noise characterization was done by repeated acquisitions of dark noise images captured under identical conditions. Main meridian analysis was accomplished by obtaining sample edge patches from the centre and near-boundary of hyperspectral image and then constructing edge and line spread functions. The final test image analysis involved verifying system calibration, image correction and compensation algorithms. Results show that with proper calibration and characterization of imaging systems, high quality images are obtained and can be used for research works which include hyperspectral image registration and hyperspectral image recognition for natural scenes.

Keywords

Hyperspectral, Imaging, Calibration

1. Introduction

Hyperspectral imaging is a technique which combines spectral and spatial imaging methods. Although the technology was developed for remote sensing it has found uses in medicine [1] [2] [3], agriculture [4] [5] [6] and art [7], just to mention a few. These non-remote systems are developed by using sensor designs different from push-broom and whisk-broom methods, commonly found in remote sensing hyperspectral imaging systems. Images are commonly acquired by mounting various electronically tunable filters in front of monochromatic cameras and capturing a range of wavelengths to produce a spectral image cube. The imaging system used for this paper falls under this category.

Illumination plays a major role during imaging, as both the camera and electronically tunable filter may suffer low transmission at the ends of the visible spectrum, resulting in a low signal to noise ratio. It is important that the spectral characteristics of the imaging system as well as its geometric properties be well characterized and its radiometric performance known. This has resulted in increased demand for characterization and calibration methodologies. For scientific research and other applications where accurate light measurement is required, the performance of the imaging system must be checked to ensure reliable data is produced.

Susana Del Pozo *et al.* [8] used vicarious methods to calibrate a multispectral imaging system on board an unmanned aerial system. Žiga Špiclin *et al.* [9] used B-spline transformation field to carry out geometric calibration on a hyperspectral imaging system. Jan Behmann *et al.* [10] geometrically calibrated hyperspectral push broom cameras in close range for plant phenotyping. Janos C. Keresztes *et al.* [11] combined calibration and glare correction techniques for real-time pixel based early apple bruise detection. Currently, there is no comprehensive method on how hyperspectral imaging systems are characterized and calibrated for natural scene imagery. This paper explores this problem.

The present work has the following structure and organization. The materials and methods used for this work are presented in Section two. These include: the hyperspectral imaging system used for acquiring images for this research, image acquisition process, input-output function computed to investigate linearity of the imaging system, analysis of system noise, main meridian analysis and calibration verification tested on Gretag Macbeth colour checker chart hyperspectral images. Results and discussion are presented in Section 3 and the conclusion is given in Section 4.

2. Materials and Methods

In this section, materials and experimental methods used for this study are presented. **Figure 1** shows a schematic diagram of the calibration and characterization of a focal-plane hyperspectral imaging system. The rest of this section describes the methods outlined in this diagram.

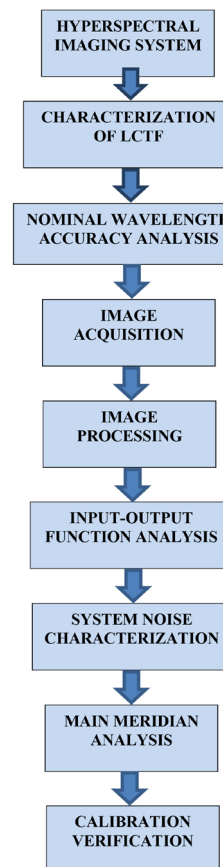


Figure 1. Schematic diagram of the calibration and characterization of a focal-plane hyperspectral imaging system.

2.1. Hyperspectral Imaging System

The system used in this research consist of a Peltier-cooled CCD camera and a liquid crystal tunable filter electronically controlled by computer software built using MATLAB programming Language. The liquid tunable filter is mounted in front of the lens with an infra-red blocking filter (**Figure 2**).

The camera is a low-noise Peltier-cooled digital camera (Hamamatsu, model C4742-95-12ER, Hamamatsu Photonics K. K., Japan). It has a resolution of 1344×1024 pixels and the available exposure times range from 10 ms to 4200 s. It uses digital temperature compensation to reduce noise since it is Peltier-cooled. The intensity response at each pixel is recorded with 12-bit precision. The spectral range is from the ultra-violet to the infra-red regions. The sensor used in the digital camera is a progressive-scan interline CCD with microlens which enables the camera to collect more photons from incoming light. It has an effective area of $8.66 \text{ mm} \times 6.60 \text{ mm}$ and sensor cell size $6.45 \mu\text{m} \times 6.45 \mu\text{m}$ (square pixels).

The liquid crystal tunable filter (LCTF) is a VariSpec, model VS-VIS2-10-HC-35-SQ, Cambridge Research and Instrumentation. It is mounted in front of the camera lens. The filter has an aperture of 35 mm and the whole imaging system has a field of view of $\pm 7^\circ$. The wavelength of peak transmission could be

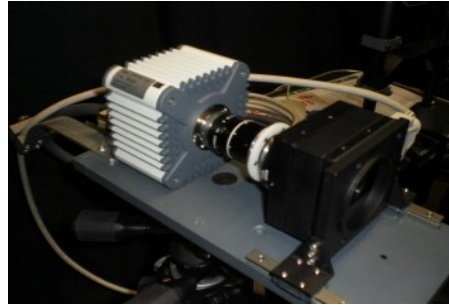


Figure 2. Hyperspectral imaging system.

varied over a range spanning 400 nm - 720 nm with a full width at half-maximum transmission of 10 nm at 550 nm, decreasing to 6 nm at 400 nm and 16 nm at 720 nm.

2.2. Nominal Wavelength Accuracy

Analysis was done to determine if the nominal wavelengths selected by the liquid crystal tunable filter and used to capture hyperspectral images are accurate. The experimental set-up involved capturing images of a mercury vapour lamp. Mercury vapour lamps have principal emission lines in the visible spectrum [12]. Two of these lines were investigated (436 nm and 546 nm). The first sets of images were captured between 420 nm and 448 nm with a 4 nm interval and the second batch were captured between 528 nm and 560 nm also having a 4 nm interval. Images were then normalised by subtracting the dark noise images and dividing by the analog camera gain and exposure time. Regions (100×100 pixels) from the image namely the centre, top right corner, middle up and top left corner were extracted, averaged and a Gaussian fit was applied respectively.

2.3. Acquisition

The process of obtaining high resolution hyperspectral images involves multiple stages. Images are generally captured by pointing the hyperspectral imaging system (CCD camera with a tunable filter mounted on it) to a scene, adjusting the focus and zoom of the CCD camera, and recording the sequences. The wavelength range used is 400 nm - 720 nm at a 10nm interval hence providing 33 images in each image sequence. Neutral grey reference materials are inserted into the scene and are used for computing the effective spectral radiance and reflectance functions of each pixel in the scene. **Figure 3** shows N2.5, N5 and N7 Munsell chips used during image acquisition.

Bespoke algorithms are used to automatically determine the exposure time of the imaging system before acquisition so that maximum pixel output is within 80% - 90% of the CCD saturation value. The spectrum of light reflected from the munsell chips are recorded immediately after acquisition by a telespectroradiometer (SpectraColorimeter, PR-650, Photo Research Inc. Chatsworth, California). For natural scene imaging, care was taken not to capture spectral images when there is movement in the scene.

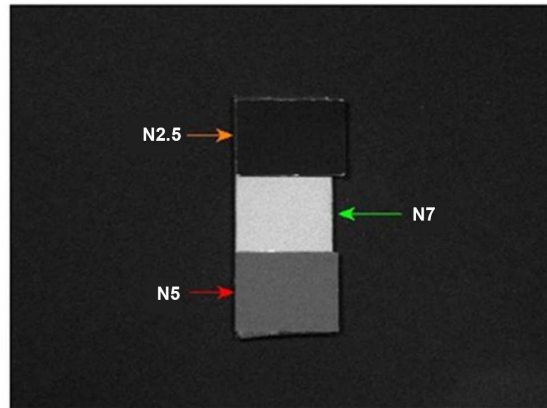


Figure 3. Munsell reference chips.

2.4. Input-Output Function

An important property of imaging systems is its linearity in response to incident light. In hyperspectral imaging systems using charge-coupled device (CCD) sensors, the basic function of the CCD is to convert photons carrying image information into an electronic signal [13]. After digitization, the signal output should ideally be linearly proportional to the amount of light incident on the sensor.

A transfer function relating the number of photons incident on the sensor and the digital output is determined by a multi-stage process which involves the creation and transfer of charge carriers (electron-hole pairs) in the active pixel regions, followed by conversion of electrons from the charge domain into the voltage domain as an amplified voltage signal. The transfer function results in a linear variation of final digitized output signal in relation to the amount of light incident on the CCD, such that the output signal is equal to the photon input multiplied by a proportionality constant (gain) [13].

The linearity of a camera system is determined by the CCD itself, as well as other electronic components in the signal processing chain. In effect, any non-linearity indicates a change in the camera's gain constant with signal level. Quantitative imaging operations rely on absolute signal measurements, and require that there be no significant interdependence between camera gain and signal intensity. Scientific CCD imaging systems exhibit good linearity over a wide signal range but when full well conditions are reached under high illumination intensity, a nonlinear response is usually observed [13]. If overall illumination is sufficiently bright, the CCD response becomes nonlinear. Depending upon the sensor characteristics, nonlinear response may also result under extremely low illumination levels.

A common technique for assessing linearity is based on a graphical plot of measured output signal as a function of exposure time, extending to the full well capacity of the device (the number of electrons held by a potential well or pixel; also referred to as linear full well) [13]. This metric may be defined as a percentage of deviation from linearity in comparison to the maximum signal intensity

obtained at full well conditions.

The linearity of the hyperspectral imaging system was investigated by recording an output-input function using a neutral density wedge, a diffuser, a beam splitter and a quartz-halogen bench lamp. This process involved measuring the signal captured by the hyperspectral imaging system and also recording the luminance using a luminance meter.

The diffuser was positioned over the aperture of the CCD camera while the neutral density wedge was placed in front of the quartz-halogen lamp and acted as a mask having a density which increases exponentially along its length. A 50/50 beam splitter made of two triangular glass prisms was placed between the light source and the hyperspectral imaging system, with the camera capturing half the signal and the luminance meter recording the other half (**Figure 4**).

Images were captured at fixed wavelengths (450 nm, 550 nm and 650 nm) as the neutral density wedge was adjusted in steps. A total of 24 steps were used ranging from bright illumination to very low light levels. The luminance meter data was recorded simultaneously. The luminance meter data was then corrected for reflection-transmission properties of the beam splitter by recording luminance meter readings from the hyperspectral imaging system position and using a linear regression fit to define a relationship between luminance meter data as seen by the hyperspectral imaging system and the original luminance meter data collected.

2.5. System Noise Characterization

The input-output function analysed in the previous section gives an indication of the linearity of the hyperspectral system but it is important to quantify the spatial variation in the sensitivity of the imaging system. In principle, the input-output data could be used for this analysis but this is not trivial, since there is no means of quantifying the spatial uniformity of the light source.

One of the aims of the characterization was to check for systematic variation from image to image in the captured series. This helps to understand the usefulness of averaging replicate images. When averaging images, the noise is assumed to be zero mean Gaussian noise. Low pass filtering of an image or averaging two images may destroy details in the image. In order to avoid such and improve the averaging technique, Mansouri *et al.* [14] acquired 6 images instead of 2 for each channel and the same process was used for this research.

Six repeated acquisitions of dark noise images were carried out under identical conditions for aperture setting 5.6 and a focus setting of infinity. A slice was then taken through the centre of each image producing intensity profiles. The slices were taken from the centre for all six images.

The other aim of this work was to analyse the relationship between the camera noise and exposure time. This analysis should give an idea of the contribution of dark current as a function of exposure time. Eight repeated acquisitions of a single wavelength (550 nm) dark noise image under identical conditions were done

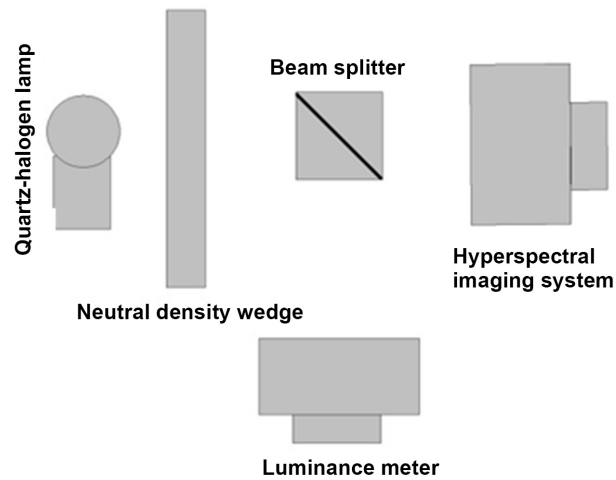


Figure 4. Input-output function experimental setup.

for aperture setting 5.6 and a focus setting of infinity. The exposure time ranged from 0.1 s to 30 s. The analog gain factor of the CCD camera was set to zero.

2.6. Main Meridian Analysis

One of the objectives of this study was to investigate the resolution of images produced by the hyperspectral imaging system in the main meridian (horizontal and vertical) at different locations in the field of view of the camera. This was accomplished by obtaining sample edge patches from the centre and near-boundary from the checker board hyperspectral image. Edge and line spread functions were constructed for these near-horizontal and near-vertical hyperspectral edges. The standard deviation from each fit was computed and recorded.

2.7. Calibration Verification

The final image analysis test involved verifying system calibration, image correction and compensation algorithms reported so far. The overall performance of the system was assessed by acquiring and processing images from a GretagMacbeth colour checker chart and then comparing the derived reflectances with those obtained with a telespectroradiometer. Reference Munsell chips N7, N5 and N2.5 were inserted at the edges of the chart (**Figure 5**). Flat field and dark noise images were also acquired. This process involved capturing six consecutive images under identical conditions, registering over position and subsequent averaging to get an image which is ideally free of temporal noise. Immediately after acquisition, the spectrum of light reflected from each patch and Munsell chips was recorded by PR650 telespectroradiometer. The averaged GretagMacbeth colour checker chart image was then corrected for dark noise and spatial non-uniformity using an averaged dark noise image and flat-field image. The image was further corrected for stray-light effects and registered over wavelength using the central wavelength image as the reference image. Spectral

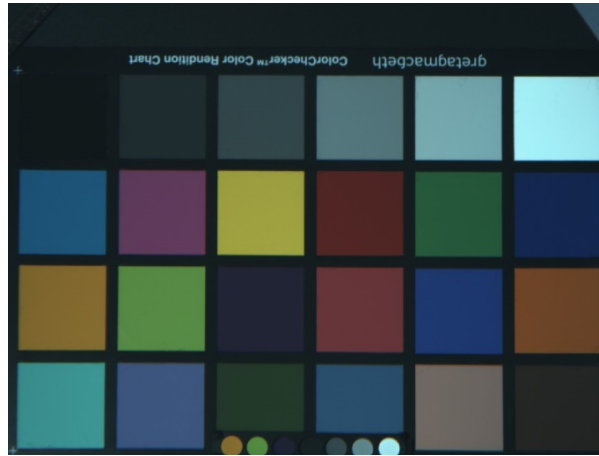


Figure 5. GretagMacbeth colour checker chart image used for calibration verification.

reflectance functions for each pixel of the corrected image was then computed by normalizing this corrected signal at each pixel against that obtained with the reference Munsell chips inserted in the scene.

3. Results and Discussion

3.1. Hyperspectral Imaging System

The spectral transmittance of the filter when varying the peak wavelength at 10 nm intervals from 400 nm to 720 nm was measured using a monochromator. **Figure 6** shows the transmittance curve for selected wavelengths (400 nm, 490 nm, 560 nm, 640 nm and 720 nm).

As can be seen from **Figure 6**, the shorter wavelength data becomes noisy after the visible spectrum. This is caused by the sensitivity of the detector inside the monochromator to these wavelengths. The characterization of the LCTF was done by plotting the nominal peak-transmission wavelength as recorded by the monochromator against the actual peak-transmission wavelengths. A Gaussian fit was first applied to the transmittance curves of the liquid crystal tunable filter measured using the monochromator to obtain peak nominal wavelengths. **Figure 7** and **Figure 8** show the plot of nominal against actual wavelength peak-transmission values and Gaussian fit for 550 nm respectively.

3.2. Nominal Wavelength Accuracy

The Gaussian fit of the central region images acquired at the short and middle wavelengths respectively are shown in **Figure 9** and **Figure 10**. The peak wavelength values from the Gaussian fit which represent the principal lines being investigated at various locations in the image are given in **Table 1**. From these results, the principal line found in the shorter wavelength region had a maximum variation of 0.6 nm while the line from the middle wavelength region had a maximum variation of 0.9 nm. These results are less than 1 nm and were

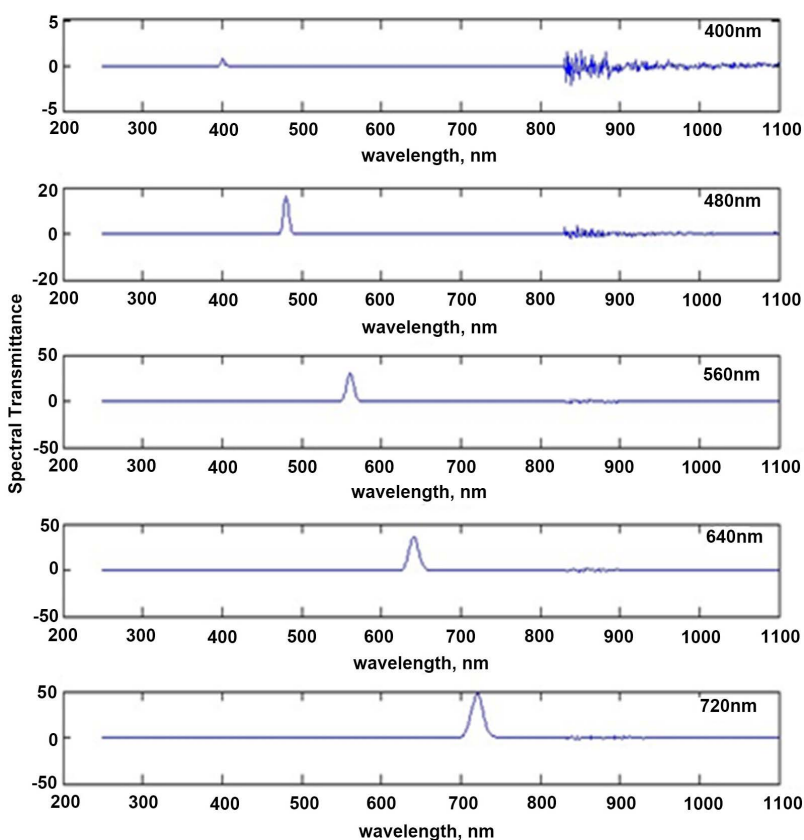


Figure 6. Spectral transmittance of a liquid crystal tunable filter measured using a monochromator.

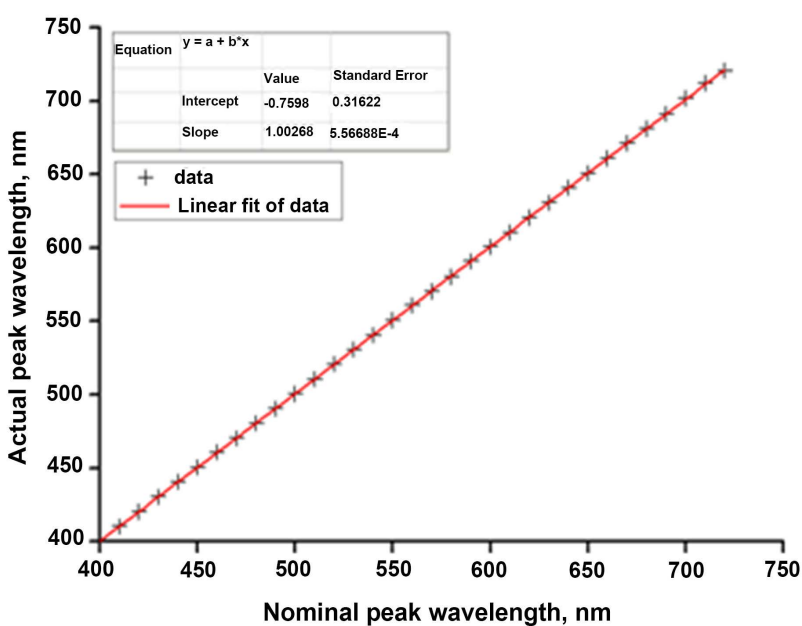


Figure 7. Plot of nominal peak wavelength against actual peak wavelength.

deemed accurate for further research work which include hyperspectral image registration and hyperspectral image scene recognition.

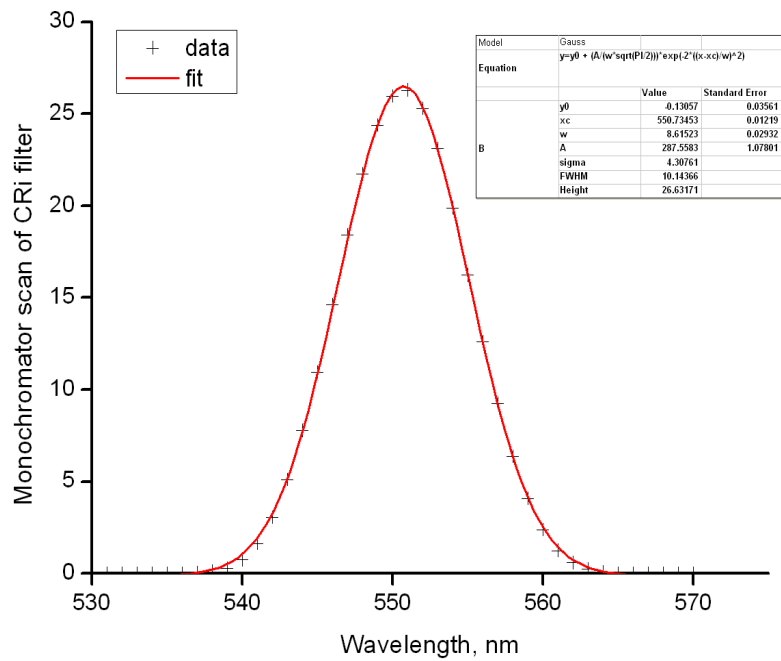


Figure 8. Gaussian fit of filter transmittance curve at 550 nm.

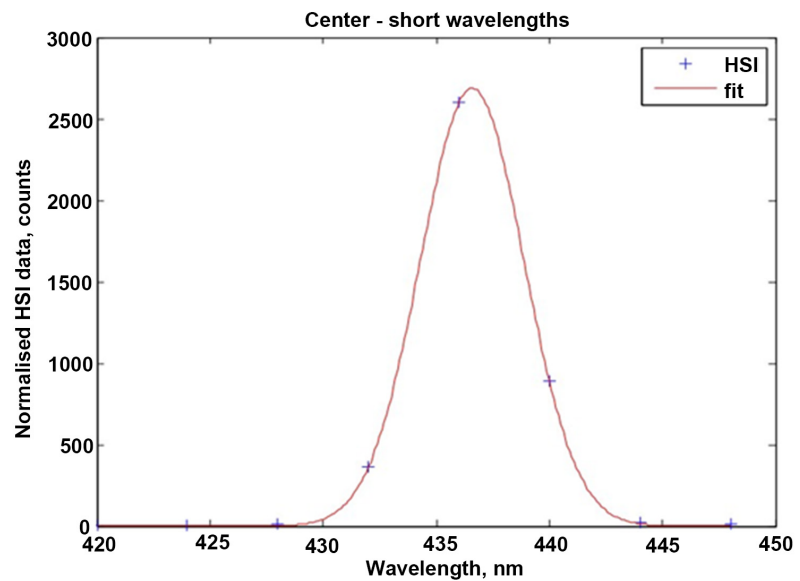


Figure 9. Gaussian fit of central region for short wavelengths (420 nm - 448 nm).

3.3. Input-Output Function

Mean signal values with pixel patches of 5×5 , 20×20 , and 790×870 were used to investigate linearity (Figure 11). These values were plotted against the normalized luminance meter data and the plot for 550 nm is given in Figure 12.

Results show the hyperspectral imaging system is linear for average light levels but the same could not be said about low light levels as the data points were too close together. This can be attributed to the property of the neutral density wedge where the density varies exponentially with length hence no significant

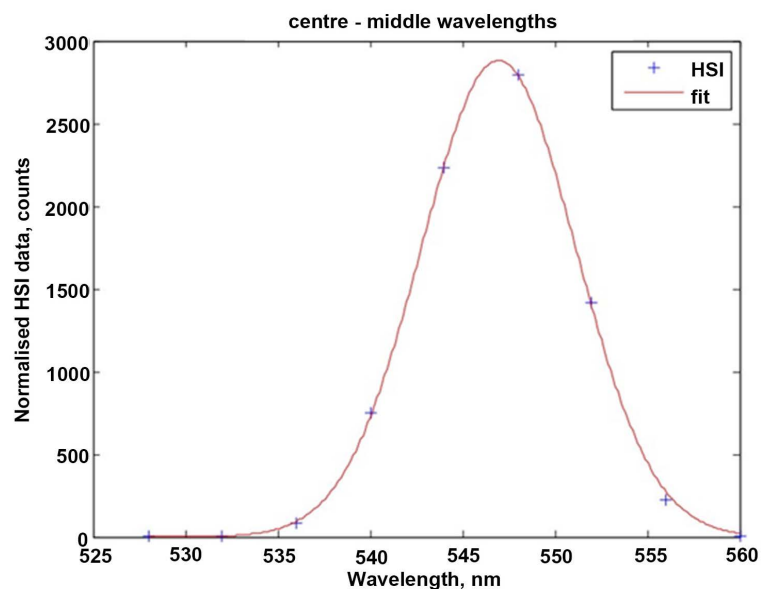


Figure 10. Gaussian fit of central region for middle wavelengths (528 nm - 560 nm).

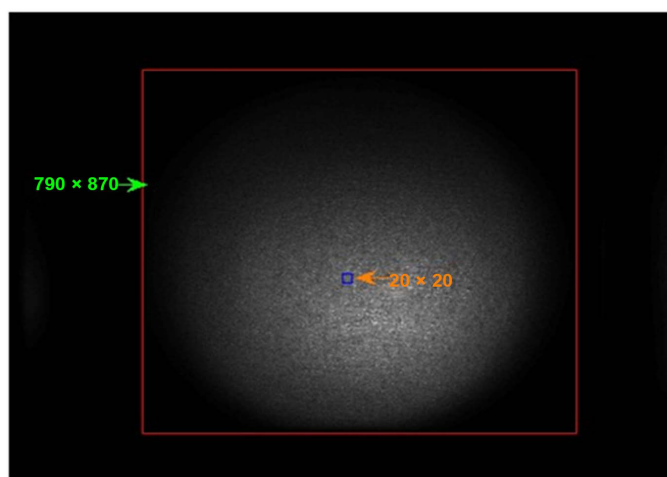


Figure 11. Test image showing 20×20 and 790×870 pixel patches.

Table 1. Mercury vapor lamp principal lines peak wavelength.

Image location	Line 1 peak Wavelength, nm	Line 2 peak Wavelength, nm
Centre	436.6	546.9
Top right corner	436.5	546.8
Top left corner	436.6	546.9
Middle up	436.6	546.5

difference as the light level reduces. An exponential fit was used to analyse the behaviour of the neutral density wedge (**Figure 13**).

Figure 13 shows that an exponential curve fits the data acquired using the neutral density wedge indicating the hyperspectral imaging system shows some form of linearity even for low light levels.

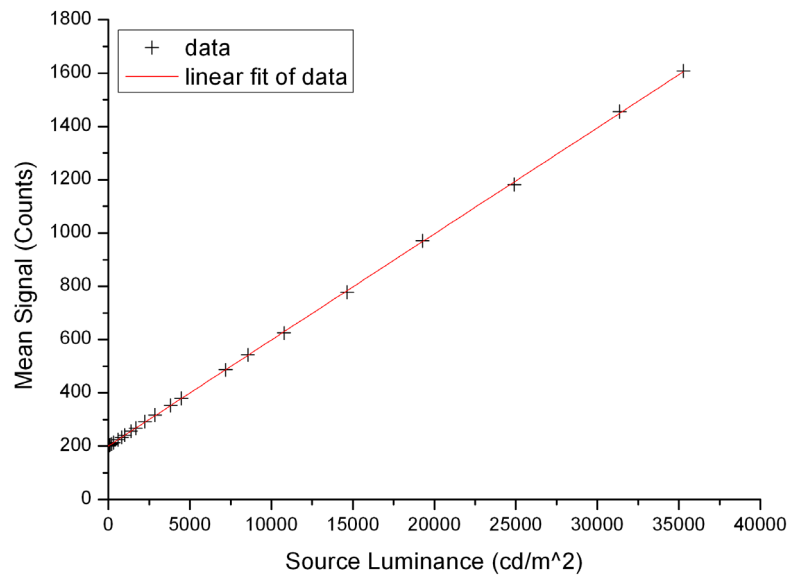


Figure 12. Mean signal of hyperspectral imaging camera against Source Luminance for 550 nm.

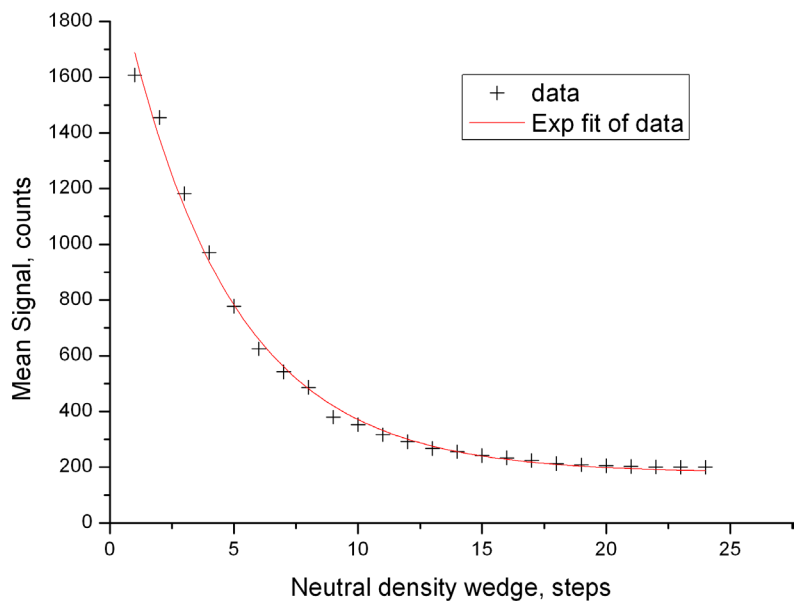


Figure 13. Exponential fit of mean signal of hyperspectral imaging camera against Source Luminance for 550 nm.

3.4. System Noise Characterization

The intensity profiles are plotted against their respective row or column sizes with one trace below the other (all six). **Figure 14** and **Figure 15** show the horizontal and vertical intensity profile plots for dark noise image acquired at 500 nm using camera aperture setting of 5.6.

From **Figure 14** and **Figure 15**, it can be seen that the fluctuations in all six images show no systematic variation which implies that an averaged image could be used for all subsequent acquisitions.

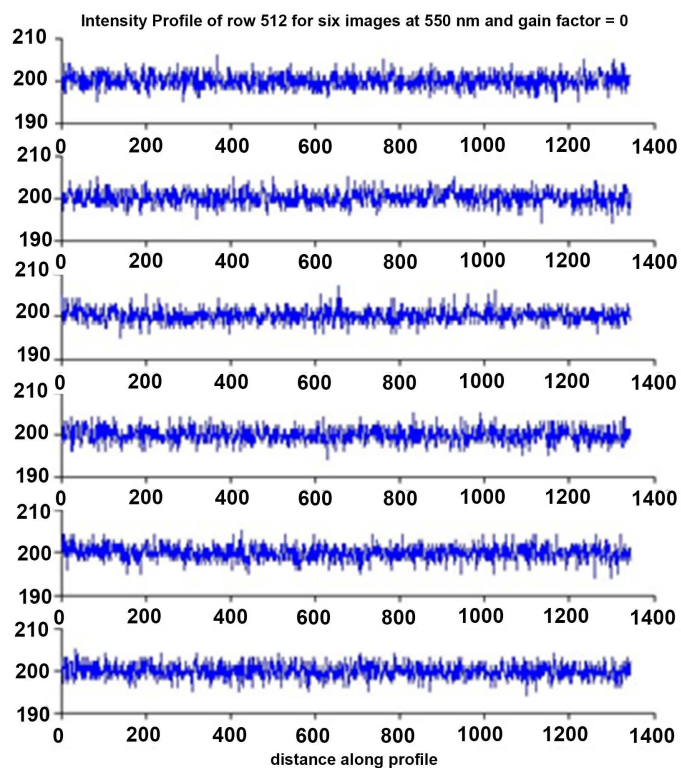


Figure 14. Horizontal slice of dark noise image captured for aperture 5.6.

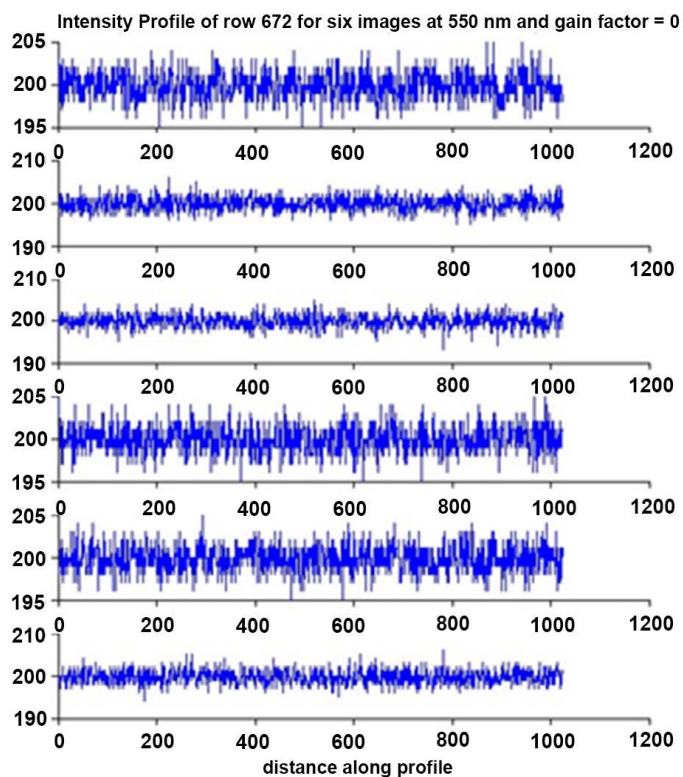


Figure 15. Vertical slice of dark noise image captured for aperture 5.6.

A plot of mean dark noise images against exposure time is given in **Figure 16**. It can be seen from **Figure 16** that the mean dark noise is almost constant over the range of exposure time used. This can be attributed to the Peltier cooling property of the CCD camera by reducing dark current noise that accumulates during extended exposure times. A plot of the standard deviation for dark noise as a function of exposure time can be seen in **Figure 17**.

3.5. Main Meridian Analysis

A plot of the standard deviation against wavelength for near-horizontal and near-vertical hyperspectral sample edge patches is presented in **Figure 18**.

Results show no significant difference between the standard deviations for horizontal and vertical edge images sampled from the centre of the image with an average standard deviation of 1.3 pixels. This result is similar with those obtained in previous work using the same hyperspectral imaging system [15]. On the other hand, the standard deviation for edges obtained from the centre and near boundaries had a significant difference. Results depend on the focus setting of the camera and vignetting at the boundaries.

3.6. Calibration Verification

A plot showing the ratio of mean signal for yellow-green and orange patches GretagMacbeth colour checker Chart is given in **Figure 19** while the ratio of purple and orange patches GretagMacbeth colour checker Chart is given in **Figure 20**. Symbols show data for the hyperspectral system and continuous lines for the telespectroradiometer.

The root mean square error in the hyperspectral estimates of reflectance across the set of test surfaces was 0.0025. Although some small systematic distortions were present in some regions of the spectrum, the overall accuracy of the

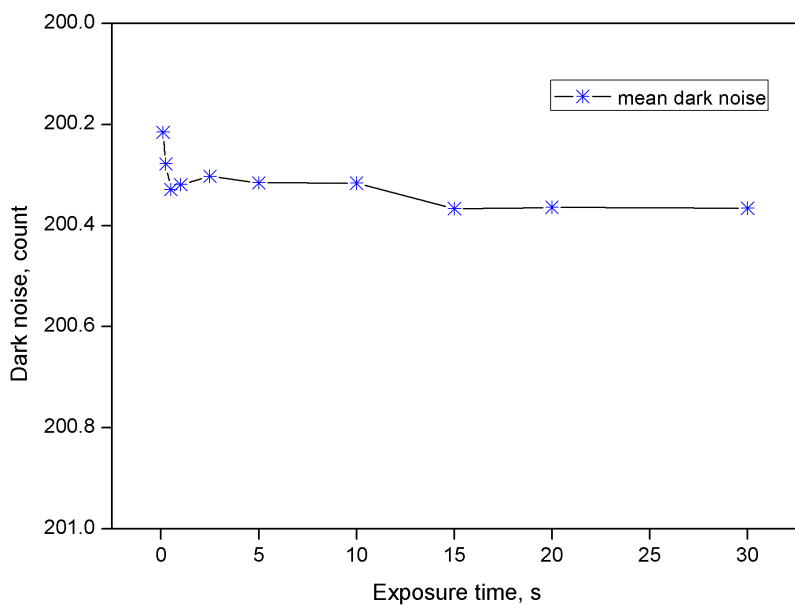


Figure 16. Plot of mean dark noise signal against exposure time.

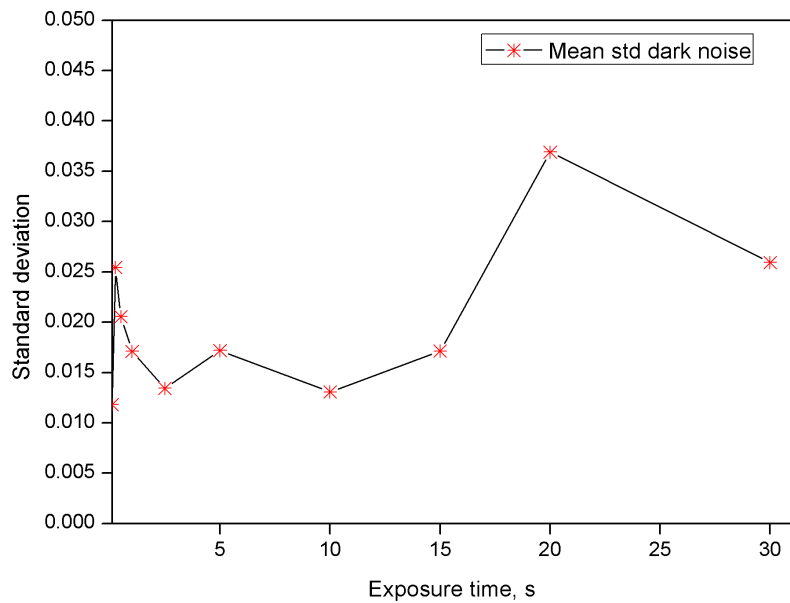


Figure 17. Plot of standard deviation of mean dark noise signal against exposure time.

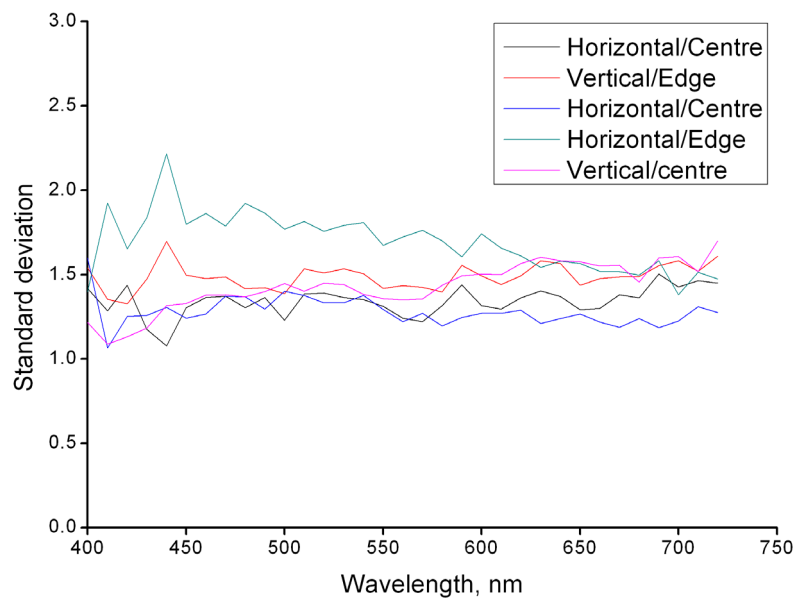


Figure 18. Plot of Line spread function (LSF) standard deviation for near-horizontal and near-vertical hyperspectral edge patches.

hyperspectral system was sufficient for further research work in natural scene imagery with emphasis on scene recognition.

4. Conclusions

This article proposes comprehensive methods for the calibration and characterization of focal-plane hyperspectral imaging systems used for natural scene imagery.

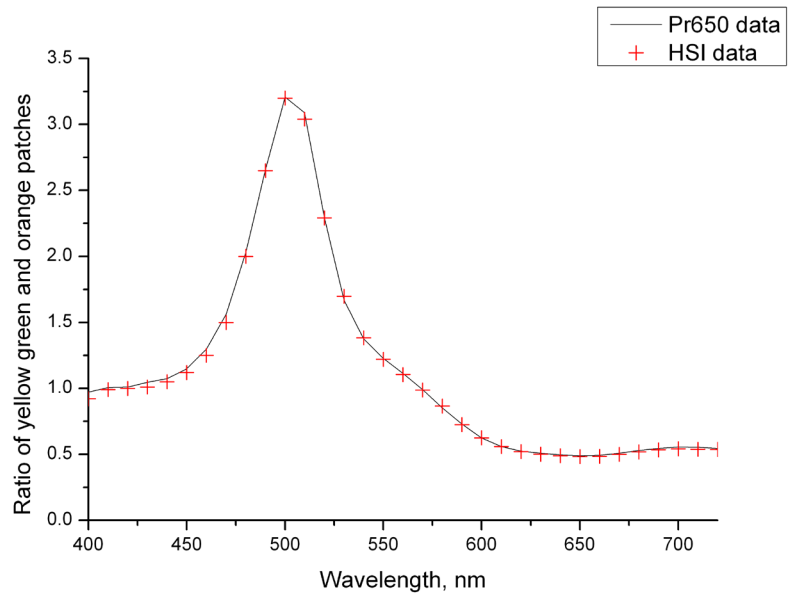


Figure 19. Spectral reflectance data for ratio between yellow-green and orange patches of GretagMacbeth colour checker chart.

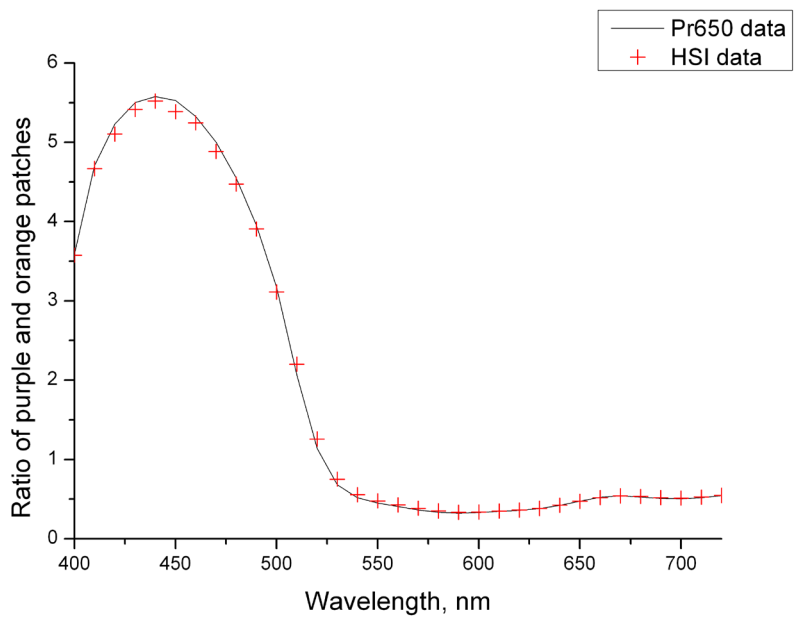


Figure 20. Spectral reflectance data for ratio between purple and orange patches of GretagMacbeth colour checker chart.

The spectral transmittance of the liquid crystal tunable filter shows the shorter wavelength data become noisy after the visible spectrum. This is caused by the sensitivity of the detector inside the monochromator to these wavelengths. This result is acceptable since we are only interested in the visible spectrum. The plot of nominal against actual wavelength peak-transmission values and Gaussian fit of transmittance curves of the liquid crystal tunable filter measured using the monochromator was very encouraging since the standard error of 0.3162 was

deemed low.

The nominal wavelength accuracy analysis shows that principal lines have a maximum variation of less than 1 nm and are accurate for further research work in natural scene imagery.

Input-output function characterization shows the hyperspectral imaging system is linear for average light levels but for low light levels, results were inconclusive as the data points were too close together. This was attributed to the property of the neutral density wedge where the density varies exponentially with length; hence no significant difference as the light level reduces. An exponential curve was used to fit the data and results show some form of linearity even for low light levels. This was encouraging since low light level presents a significant problem in hyperspectral imaging.

System noise characterization shows that the fluctuations in repeated images show no systematic variation which implies that an averaged image could be used for all subsequent acquisitions and image correction. A systematic variation normally means there is a problem with the imaging system.

Main meridian analysis results show no significant difference between the standard deviations for horizontal and vertical edge images sampled from the centre of the image with an average standard deviation of 1.3 pixels. The standard deviation for edges obtained from near boundaries had higher values with some reaching 2.1 pixels. Focus setting and vignetting play a major role in determining results at the boundaries. Future work will find ways to tackle this problem.

Finally, the performance of the proposed methods was evaluated by calibration verification of a GretagMacbeth colour checker chart hyperspectral image. The root mean square error in the hyperspectral estimates of reflectance across the set of test surfaces was 0.0025. Results show the overall accuracy of the hyperspectral system was sufficient for further research work in natural scene imagery with emphasis on scene recognition.

Conflicts of Interest

The author declares no conflicts of interest regarding the publication of this paper.

References

- [1] Susanne, P., Karina, W., Jürgen, P., Bayden, R.W., Kamila, K., Anja, R., Perez-Guaita, D., Philip, H., Nick, S., Alex, D., Ben, G., Rohith, R., David, M. and Rohit, B. (2018) Application of Vibrational Spectroscopy and Imaging to Point-of-Care Medicine: A Review. *Applied Spectroscopy*, **72**, 52-84.
- [2] Calin, M.-A., Coman, T., Viorel Parasca, S., Bercau, N., Savastru, R.S. and Manea, D. (2015) Hyperspectral Imaging-Based Wound Analysis Using Mixture-Tuned Matched Filtering Classification Method. *Journal of Biomedical Optics*, **20**, Article ID: 046004. <https://doi.org/10.1117/1.JBO.20.4.046004>
- [3] Fei, B., *et al.* (2017) Label-Free Hyperspectral Imaging and Quantification Methods

for Surgical Margin Assessment of Tissue Specimens of Cancer Patients. 2017 39th Annual International Conference of the IEEE Engineering in Medicine and Biology Society (EMBC), Seogwipo, 11-15 July 2017, 4041-4045.

<https://doi.org/10.1109/EMBC.2017.8037743>

- [4] Lankapalli, R., Digvir, S.J., Noel, D.G.W., Paul, G.F. and Da-Wen, S. (2017) Extraction of Spectral Information from Hyperspectral Data and Application of Hyperspectral Imaging for Food and Agricultural Products. *Food and Bioprocess Technology*, **10**, 1-33.
- [5] Liu, L., Li, M., Liu, W., Zhao, Z. and Liu, X. (2018) Application of Hyperspectral Imaging Technology in Nondestructive Testing of Fruit Quality. *Proceedings of Tenth International Conference on Information Optics and Photonics*, 109646E. <https://doi.org/10.1117/12.2506528>
- [6] Adão, T., Hruška, J., Pádua, L., Bessa, J., Peres, E., Morais, R. and Sousa, J.J. (2017) Hyperspectral Imaging: A Review on UAV-Based Sensors, Data Processing and Applications for Agriculture and Forestry. *Remote Sensing*, **9**, 1110. <https://doi.org/10.3390/rs9111110>
- [7] Polak, A., Kelman, T., Murray, P., Marshall, S., Stothard, D.J.M., Eastaugh, N. and Eastaugh, F. (2017) Hyperspectral Imaging Combined with Data Classification Techniques as an Aid for Artwork Authentication. *Journal of Cultural Heritage*, **26**, 1-11.
- [8] Susana, D.P., Pablo, R.-G., Hernandez, D. and Felipe, B. (2014) Vicarious Radiometric Calibration of Multispectral Camera on Board Unmanned Aerial System. *Remote Sensing*, **6**, 1918-1937. <https://doi.org/10.3390/rs6031918>
- [9] Špiclin, Ž., Katrašnik, J., Bürmen, M., Pernuš, F. and Likar, B. (2010) Geometric Calibration of a Hyperspectral Imaging System. *Applied Optics*, **49**, 2813-2818. <https://doi.org/10.1364/AO.49.002813>
- [10] Behmann, J., et al. (2015) Calibration of Hyperspectral Close-Range Pushbroom Cameras for Plant Phenotyping. *ISPRS Journal of Photogrammetry and Remote Sensing*, **106**, 172-182. <https://doi.org/10.1016/j.isprsjprs.2015.05.010>
- [11] Keresztes, J.C., Goodarzi, M. and Saeys, W. (2016) Real-Time Pixel Based Early Apple Bruise Detection Using Short Wave Infrared Hyperspectral Imaging in Combination with Calibration and Glare Correction Techniques. *Food Control*, **66**, 215-226. <https://doi.org/10.1016/j.foodcont.2016.02.007>
- [12] Wyszecki, G. and Stiles, W.S. (2000) Color Science: Concepts and Methods, Quantitative Data and Formulae. John Wiley & Sons, Hoboken, NJ.
- [13] Gerald, C. (1996) Holst. CCD Arrays, Cameras, and Displays. SPIE Optical Engineering Press and JCD Publishing, Washington DC.
- [14] Mansouri, A., Marzani, F.S. and Gouton, P. (2005) Development of a Protocol for CCD Calibration: Application to a Multispectral Imaging System. *International Journal of Robotics and Automation*, **20**, 94-100. <https://doi.org/10.2316/Journal.206.2005.2.206-2784>
- [15] Foster, D.H., Amano, K., Nascimento, S.M.C. and Foster, M.J. (2006) Frequency of Metamerism in Natural Scenes. *Journal of the Optical Society of America A*, **23**, 2359-2371. <https://doi.org/10.1364/JOSAA.23.002359>